

Photothermal and photoacoustic Raman cytometry *in vitro* and *in vivo*

Evgeny V. Shashkov,^{1,2} Ekaterina I. Galanzha,¹ and Vladimir P. Zharov^{1*}

¹Phillips Classic Laser and Nanomedicine Laboratories,
University of Arkansas for Medical Sciences, 4301 W. Markham,
Little Rock, AR, 72205, USA

²Prokhorov General Physics Institute,
Moscow 119991, Russia

*zharovvladimirp@uams.edu

Abstract: An integrated Raman-based cytometry was developed with photothermal (PT) and photoacoustic (PA) detection of Raman-induced thermal and acoustic signals in biological samples with Raman-active vibrational modes. The two-frequency, spatially and temporally overlapping pump–Stokes excitation in counterpropagating geometry was provided by a nanosecond tunable (420–2300 nm) optical parametric oscillator and a Raman shifter (639 nm) pumped by a double-pulsed Q-switched Nd:YAG laser using microscopic and fiberoptic delivery of laser radiation. The PA and PT Raman detection and imaging technique was tested *in vitro* with benzene, acetone, olive oil, carbon nanotubes, chylomicron phantom, and cancer cells, and *in vivo* in single adipocytes in mouse mesentery model. The integration of linear and nonlinear PA and PT Raman scanning and flow cytometry has the potential to enhance its chemical specificity and sensitivity including nanobubble-based amplification (up to 10- fold) for detection of absorbing and nonabsorbing targets that are important for both basic and clinically relevant studies of lymph and blood biochemistry, cancer, and fat distribution at the single-cell level.

©2010 Optical Society of America

OCIS codes: (190.4380) Nonlinear optics; (300.6230) Spectroscopy, coherent anti-Stokes Raman scattering; (350.5340) Photothermal effects; (170.1530) Cell analysis; (350.4990) Particles.

References and links

1. V. P. Zharov, and V. S. Letokhov, *Laser Optoacoustic Spectroscopy* (Springer-Verlag; Berlin Heidelberg 1986).
2. V. P. Zharov, *Laser optoacoustic spectroscopy in chromatography*: in *Laser Analytical Spectrochemistry*, V. S. Letokhov, ed. (Boston, 1986), pp. 229–271.
3. M. Xu, and L. V. Wang, “Photoacoustic imaging in biomedicine,” *Rev. Sci. Instrum.* **77**(4), 041101 (2006).
4. L. V. Wang, ed., *Photoacoustic imaging and spectroscopy* (CRC Press, 2009).
5. J. W. Kim, E. I. Galanzha, E. V. Shashkov, H. M. Moon, and V. P. Zharov, “Golden carbon nanotubes as multimodal photoacoustic and photothermal high-contrast molecular agents,” *Nat. Nanotechnol.* **4**(10), 688–694 (2009).
6. E. I. Galanzha, E. V. Shashkov, T. Kelly, J.-W. Kim, L. Yang, and V. P. Zharov, “In vivo magnetic enrichment and multiplex photoacoustic detection of circulating tumour cells,” *Nat. Nanotechnol.* **4**(12), 855–860 (2009).
7. V. P. Zharov, E. I. Galanzha, E. V. Shashkov, J.-W. Kim, N. G. Khlebtsov, and V. V. Tuchin, “Photoacoustic flow cytometry: principle and application for real-time detection of circulating single nanoparticles, pathogens, and contrast dyes in vivo,” *J. Biomed. Opt.* **12**(5), 051503 (2007).
8. E. I. Galanzha, E. V. Shashkov, P. M. Spring, J. Y. Suen, and V. P. Zharov, “In vivo, noninvasive, label-free detection and eradication of circulating metastatic melanoma cells using two-color photoacoustic flow cytometry with a diode laser,” *Cancer Res.* **69**(20), 7926–7934 (2009).
9. S. Nechaev and N. Ponomarev, “High-resolution Raman spectrometer,” *Sov. J. Quantum Electron.* **5**, 72–76 (1975).
10. J. J. Barrett, and M. J. Berry, “Photoacoustic Raman spectroscopy (PARS) using cw laser sources,” *Appl. Phys. Lett.* **34**(2), 144–147 (1979).

11. C. K. N. Patel, and A. C. Tam, "Optoacoustic Raman gain spectroscopy of liquids," *Appl. Phys. Lett.* **34**(11), 760–763 (1979).
12. A. C. Tam, "Applications of photoacoustic sensing techniques," *Rev. Mod. Phys.* **58**(2), 381–431 (1986).
13. G. A. West, D. R. Siebert, and J. J. Barrett, "Gas phase photoacoustic Raman spectroscopy using pulsed laser excitation," *Appl. Phys. (Berl.)* **51**, 2823–2828 (1980).
14. J. J. Barrett, and D. F. Heller, "Theoretical analysis of photoacoustic Raman spectroscopy," *J. Opt. Soc. Am.* **71**(11), 1299–1308 (1981).
15. C. K. N. Patel, and A. C. Tam, "Pulsed optoacoustic spectroscopy of condensed matter," *Rev. Mod. Phys.* **53**(3), 517–550 (1981).
16. A. M. Brodnikovskii, V.P. Zharov, and N.P. Koroteev, "Photoacoustic Raman spectroscopy of molecular gases," *Sov. J. Quantum Electron.* **•••**, 2421–2430 (1985).
17. Y. Oki, N. Kawada, T. Ogawa, Y. Abe, and M. Maeda, "Y. Abe and M. Maeda, "Sensitive H₂ detection using a new technique of photoacoustic Raman spectroscopy," *Jpn. J. Appl. Phys.* **36**(Part 2, No. 9A/B), L1172–L1174 (1997).
18. K. Das, Y. Rostovtsev, K. Lehmann, and M. Scully, "Thermodynamic and noise considerations for the detection of microscopic particles in a gas by photoacoustic Raman spectroscopy," *Opt. Commun.* **246**(4-6), 551–559 (2005).
19. Y. Oki, S. Nakazono, Y. Nonaka, and M. Maeda, "Sensitive H₂ detection by use of thermal-lens Raman spectroscopy without a tunable laser," *Opt. Lett.* **25**(14), 1040–1042 (2000).
20. Y. Oki, N. Kawada, Y. Abe, and M. Maeda, "Nonlinear Raman spectroscopy without tunable laser for sensitive gas detection in the atmosphere," *Opt. Commun.* **161**(1-3), 57–62 (1999).
21. R. C. Sharma, "A novel demonstration of photoacoustic Raman spectroscopy with combined stimulated Raman pumping in H₂ molecule," *Opt. Commun.* **282**(6), 1183–1185 (2009).
22. A. M. Sakashita, S. P. Bydlowski, D. A. F. Chamone, and R. C. Maranhão, "Plasma kinetics of an artificial emulsion resembling chylomicrons in patients with chronic lymphocytic leukemia," *Ann. Hematol.* **79**(12), 687–690 (2000).
23. Y. Park, W. J. Grellner, W. S. Harris, and J. M. Miles, "A new method for the study of chylomicron kinetics in vivo," *Am. J. Physiol. Endocrinol. Metab.* **279**(6), E1258–E1263 (2000).
24. J.-W. Kim, E. V. Shashkov, E. I. Galanzha, N. Kotagiri, and V. P. Zharov, "Photothermal antimicrobial nanotherapy and nanodiagnosics with self-assembling carbon nanotube clusters," *Lasers Surg. Med.* **39**(7), 622–634 (2007).
25. E. I. Galanzha, V. V. Tuchin, and V. P. Zharov, "Advances in small animal mesentery models for in vivo flow cytometry, dynamic microscopy, and drug screening," *World J. Gastroenterol.* **13**(2), 192–218 (2007).
26. V. P. Zharov, and D. O. Lapotko, "Photothermal imaging of nanoparticles and cells," *IEEE J. Sel. Top. Quantum Electron.* **11**(4), 733–751 (2005).
27. R. M. El-Abassy, P. Donfak, and A. Materny, "Visible Raman spectroscopy for the discrimination of olive oils from different vegetable oils and the detection of adulteration," *J. Raman Spectrosc.* **•••**, 2279 (2009).
28. C. Heinrich, A. Hofer, A. Ritsch, C. Ciardi, S. Bernet, and M. Ritsch-Marte, "Selective imaging of saturated and unsaturated lipids by wide-field CARS-microscopy," *Opt. Express* **16**(4), 2699–2708 (2008).
29. A. S. Biris, E. I. Galanzha, Z. Li, M. Mahmood, Y. Xu, and V. P. Zharov, "In vivo Raman flow cytometry for real-time detection of carbon nanotube kinetics in lymph, blood, and tissues," *J. Biomed. Opt.* **14**(2), 021006 (2009).
30. J. De Gelder, K. De Gussem, P. Vandenaabeele, and L. Moens, "References database of Raman spectra of biological molecules," *J. Raman Spectrosc.* **38**(9), 1133–1147 (2007).
31. V. Capozzi, G. Perna, A. Gallone, P. F. Biagi, P. Carmone, A. Fratello, G. Guida, P. Zanna, and R. Cicero, "Raman and optical spectroscopy of eumelanin films," *J. Mol. Struct.* **744-747**, 717–721 (2005).
32. T. T. Le, T. B. Huff, and J. X. Cheng, "Coherent anti-Stokes Raman scattering imaging of lipids in cancer metastasis," *BMC Cancer* **9**(1), 42 (2009).
33. V. P. Zharov, V. Galitovskiy, C. S. Lyle, and T. C. Chambers, "Superhigh-sensitivity photothermal monitoring of individual cell response to antitumor drug," *J. Biomed. Opt.* **11**(6), 064034 (2006).
34. C. Heinrich, C. Meusburger, S. Bernet, and M. Ritsch-Marte, "CARS microscopy in a wide-field geometry with nanosecond pulses," *J. Raman Spectrosc.* **37**(6), 675–679 (2006).
35. X. Nan, J. X. Cheng, and X. S. Xie, "Vibrational imaging of lipid droplets in live fibroblast cells with coherent anti-Stokes Raman scattering microscopy," *J. Lipid Res.* **44**(11), 2202–2208 (2003).

Introduction

Photothermal (PT) and photoacoustic (PA) methods employing nonradiative conversion of absorbed energy into heat and sound have successfully been used in spectroscopy, microscopy, analytical chemistry, biology, and medicine (e.g., [1–6]). Conventional PA/PT spectroscopy in the visible and near-infrared (NIR) spectral ranges is based on optical non-excitation of electronic and vibrational modes of natural chromophores (e.g., cytochromes, melanin, and hemoglobin) or synthetic absorbing micro- and nanoparticles as PA/PT contrast agents. In particular, we demonstrated the capability of linear PT and PA cytometry in

scanning and flow modes to detect individual cells, bacteria, and nanoparticles *in vitro* and *in vivo* in blood and lymph flow at sensitivity thresholds that are unachievable with existing techniques [5–8]. The selective detection *in vivo* of rare cells of interest (e.g., metastatic tumor cells) presents a challenge because of the complex biological absorption background. To spectrally identify fast flowing cells, we developed a time-resolved linear PA two-color cytometer, using two nanosecond laser pulses at selected wavelengths and delay times [6–8]. These pulses were activated by the third (355 nm) and second (532 nm) harmonics of an Nd:YAG laser which pumped to an optical parametric oscillator (OPO) with a tunable spectral range of 420–2300 nm and a Raman shifter with a fixed wavelength of 639 nm, respectively. Here we show that this technique, after further modification, can provide a method of *in vivo* nonlinear PA and PT Raman cytometry with chemical specificity. This can be achieved by PT and PA detection of Raman-induced heat and sound in either the nonabsorbing or absorbing cells with Raman-active vibrational modes.

Historically, the nonlinear spectroscopic technique combining stimulated Raman scattering with acoustic detection, referred to as PA Raman spectroscopy (PARS), was first suggested in 1975 by Nechaev and Ponomarev [9]. The technique was first employed in 1979 in gas by Barrett and Berry [10] using two continuous-wave (CW) or nanosecond pulse lasers. Nonbiological liquids were studied by Patel and Tam using microsecond laser pulses [11,12]. Later application of PARS was focused mainly on gas analysis [e.g., 13–21]. In particular, we demonstrated the capability of PARS with counterpropagating geometry of Stokes and pump beams (i.e., pump positioned in the forward direction and Stokes positioned in a backwards direction) increased the sensitivity and especially specificity of trace analysis in gaseous mixtures, using two nanosecond pulses from an Nd:YAG laser (second harmonic, 532 nm) and a tunable dye laser (545–630 nm) [16]. In these and other studies, nonlinear PARS techniques were used separately from conventional linear PA spectroscopy, and the laser energy level was relatively high that it could damage biological samples. Here we propose the integration of linear and nonlinear PA and PT Raman cytometry (PARC and PTRC, respectively) that may allow detection, with chemical specificity, both absorbing and weakly absorbing cells simultaneously at a laser energy level safe for biological tissues. We present a brief discussion of the theory underlying these techniques, optical scheme features, parameter testing with conventional nonbiological samples, and proof-of-concept, using normal and cancer cells *in vitro* and *in vivo*. The advantages, limitations, and further improvement of this new optical technology are also discussed.

Materials and methods

Principles of PT and PA Raman cytometry

Conventional linear PA and PT cytometry (which we will refer to as PA/PT until noted) is based on the direct detection of light absorption in a sample. Nonlinear PA/PT Raman technique is based on stimulated Raman scattering phenomena leading eventually to the generation of heat and sound (i.e., it is not necessary for light to be directly absorbed by the sample). Cells with Raman-active vibrational modes are simultaneously irradiated with two spatially and temporally overlapping laser pulses: the pump beam, with a relatively high frequency ν_P and energy E_P , induces Raman scattering; and the Stokes (or signal) beam with a lower frequency ν_S and energy E_S , acts as a wave at the Stokes frequency [Fig. 1(a)].

The Stokes photon energy level is lower than the pump photon level (i.e., $h\nu_S < h\nu_P$). If $\nu_P - \nu_S$ is close to a Raman-active frequency (transition), ν_R of a cell (i.e., $\nu_R \approx \nu_P - \nu_S$), during nonlinear interaction through the third-order nonlinear susceptibility, Raman gain occurs; that is, the pump beam is attenuated, and the Stokes beam is amplified, photon for photon [12]. In other words, the pump photon energy level induces transitions from a background state to a virtual state (which could also coincides with an actual state of the cell or other cells) and

then to an excited state. The energy from an excited state can be converted through radiative relaxation to fluorescence or through nonradiative relaxation to translational energy via molecular collision, i.e., into heat and accompanying acoustic waves (i.e., as in conventional linear PA spectroscopy) that can be detected by the PT (e.g., thermolens) or PA techniques [Fig. 1(b)].

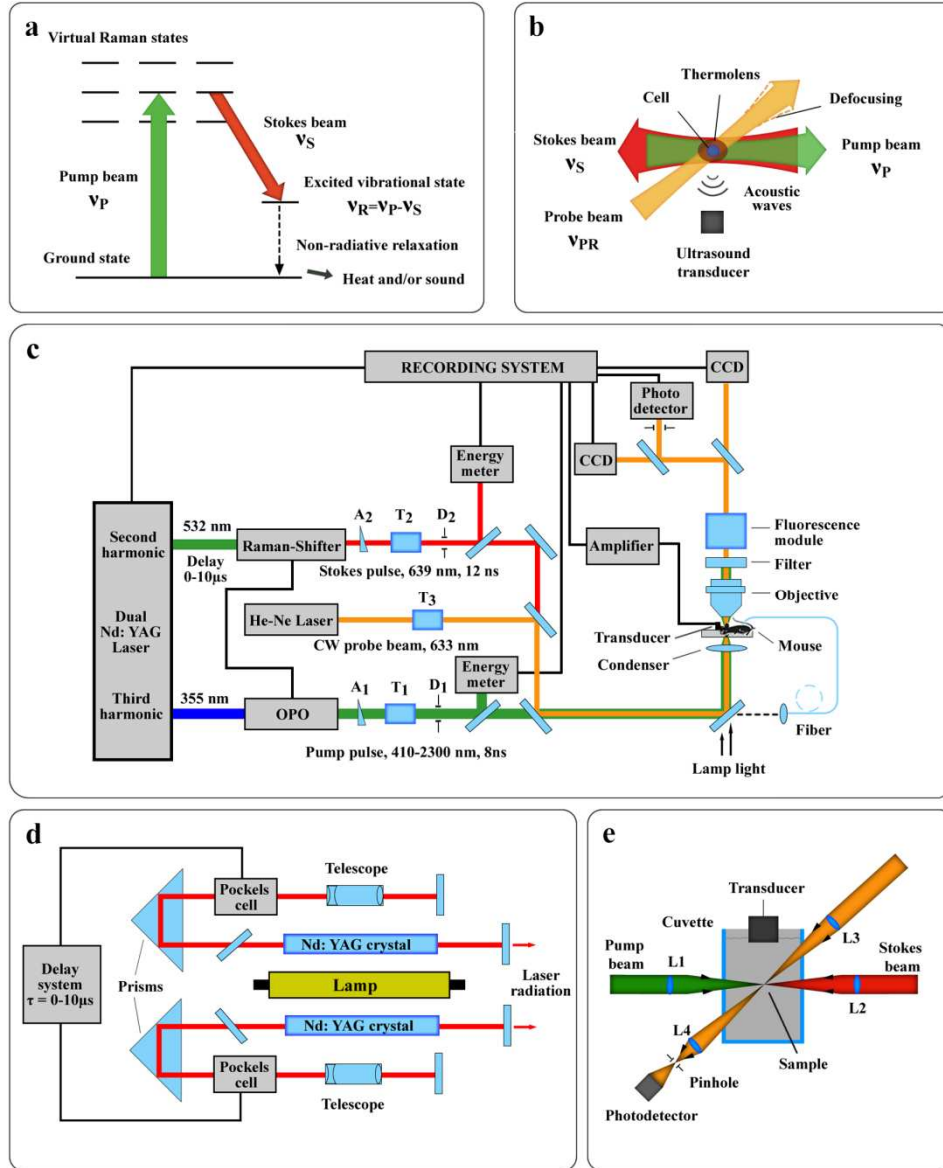


Fig. 1. Method of PA and PT Raman cytometry with two-frequency excitation of the vibrational mode of the cells. (a) Level scheme of the Raman transition. (b) Schematic of cell irradiation. (c) Microscopic and fiber-based optical diagram. T, telescope; D, diaphragm; A, attenuator. (d) Double pumping of two-channel Nd:YAG laser. (e) Scheme details.

For each photon conversion from the pump beam to the Stokes beam, the amount of energy $h(\nu_p - \nu_s) = h\nu_R$ is lost from the optical beams and is deposited in the medium. The number of photons that have undergone conversion is then $\Delta E_S / (h\nu_S)$. Hence, the total energy

deposited in the medium is $\Delta E_R = \Delta E_S(\nu_R/\nu_S)$. At the typically low Raman-gain coefficient g_S ($g_S L \ll 1$), total energy release ΔE can be described simply as follows [1]:

$$\Delta E / L = [(\nu_p - \nu_s) / \nu_s] E_s g_s + E_p \alpha_s + E_p \alpha_p, \quad (1)$$

where gain g_S is proportional to the spontaneous Raman scattering cross-section σ_R , pump pulse energy E_p , and some specific cell parameters [12]; L is the gain path length (i.e., effective length of interaction between the sample and the pump and Stokes beams); and α_s and α_p are the absorption coefficients in the sample at the frequencies ν_p and ν_s . As a result, the PA/PT signals, which are proportional to the ratio $\Delta E/L$, consist of nonlinear Raman-related components (first term in Eq. (1) and two linear PA signals as a result of absorption of laser radiation in cells at the frequencies ν_p and ν_s (second and third terms in Eq. (1), respectively). Thus, a nonlinear Raman signal is proportional to the ratio $E_s E_p / (t_p A_p)$ [12], where t_p is the duration of the pump beam and A_p is the cross-sectional effective area of the pump beam (assuming exact spatial overlap of the pump and the Stokes beams). To increase the signal, t_p and A_p must be decreased at constant energies E_s and E_p . In cytometric applications, parameter L is comparable to the size of single cells or a Raman-active intracellular zone (e.g., organelles or biomolecule clusters). Spectral resolution is determined by the total spectral width (convolution) of the laser radiation at the frequencies ν_p and ν_s . Spectral line shapes of PA/PT Raman spectra are similar to those in conventional Raman scattering technique.

Sample preparation

For testing and calibration purposes, we used benzene, acetone (99.6% A929-4, Fisher Scientific), and olive oil (Extra Virgin, Cold Pressed Olive Oil, Pure, distributed by the KROGER CO., Cincinnati, Ohio 45202). Chylomicron phantoms measuring $\sim 0.2 \mu\text{m}$ in diameter were prepared according to standard procedures [22,23]. Specifically, the mix, which consisted of vegetable oil (10%), bovine serum albumin (5%), and glycerol (2.5%) in phosphate-buffered saline (PBS) (87.5%), was subjected to sonic agitation for 5 minutes, ultracentrifuged at 40,000 rpm for 30 minutes, and then filtered with a $0.2\text{-}\mu\text{m}$ filter. The sample was kept at -20°C .

Single-walled carbon nanotubes (CNTs; Carbon Nanotechnologies Inc., Houston, TX) were processed as described previously [5,24]. Their average length and diameter were 186 nm and 1.7 nm at a concentration of 22 $\mu\text{g}/\text{mL}$ in PBS.

B16F10 mouse melanoma cells and WTY-1 human breast cancer cells (American Type Culture Collection, Manassas, VA) were cultured according to the vendor's specifications (e.g., see [8]). Viable cells were resuspended in PBS for all tests.

Animals

Nude *nu/nu* mice weighing 20–25 g (Harlan Sprague-Dawley, Indianapolis, IN) were used to obtain the PA and PT Raman signals from adipocytes in mouse mesentery in accordance with protocols approved by the University of Arkansas for Medical Sciences Institutional Animal Care and Use Committee. After standard anesthesia by intraperitoneal injection of ketamine/xylazine (50 mg/10 mg/kg), mice were laparotomized by a small midabdominal incision, and the intestinal mesentery was placed on a customized, heated (37.7°C) microscope stage and suffused with warmed Ringer's solution (37°C , pH 7.4) containing 1% albumin to prevent protein loss. In a conventional optical scheme, the mesentery was also submerged in an optical cuvette containing warmed PBS. The mesentery provides a minimally invasive but well-established *in vivo* model. No marked changes in tissue, microvessel morphology, or cell-flow dynamics were seen for at least 5 h of observation and over periods of repeated observation extending up to 2 months [25]. Because of the thin,

transparent mesenteric structure, this model represents a “gold standard” for providing first-step verification of this novel technology.

Experimental setup

The setup was built on the platform of an upright Olympus BX51 microscope that integrates PA, PT, fluorescence, transmission digital microscopy (TDM), and fiberoptic modules [Fig. 1(c)], as previously described [5–8, 26]. A tunable OPO (LT- 2214PC, Lotis Ltd., Minsk, Belarus) provided a pulsed pump beam with the following parameters: wavelength, 420–2300 nm; pulse width (FWHM), 8 ns; adjustable beam diameter, 10–100 μm ; beam divergence, ~ 6 mrad; maximum pulse energy, 5 mJ; fluence range, $1\text{--}10^4$ mJ/cm^2 per pulse; line width, ~ 0.5 nm; polarization signal and idle wave, horizontal; and pulse repetition rate, 10 Hz. The OPO wavelength was controlled with a spectrometer (USB 4000-VIS-NIR) from Ocean Optics (Dunedin, FL). A solid-state Raman shifter (LZ 221, SOLAR Laser System, Minsk, Belarus) provided the Stokes beam with the following parameters: fixed wavelength, 639 nm; pulse width (FWHM), 12 ns; beam divergence, ~ 8 mrad; maximum pulse energy, 4 mJ; fluence range, $1\text{--}10^4$ mJ/cm^2 per pulse; polarization, horizontal; line width, ~ 0.5 nm; and pulse repetition rate, 10 Hz. The OPO and the Raman shifter were pumped by the second (532 nm) and third (355 nm) harmonics, respectively, of a double-pulsed Q-switched Nd:YAG laser, in which one flash-lamp simultaneously excited two laser crystals [Fig. 1(d)]. This system simultaneously provided two laser pulses with a small jitter (1–2 ns) that is critical for accurate temporal synchronization of the pump and Stokes beams as required for effective generation of nonlinear PA/PT Raman signals. We used an OPO tunable in the visible spectral range (420–600 nm) as the pump beam and a Raman shifter fixed at 639 nm as the Stokes beam, as well as the converse: the Raman shifter fixed at 639 nm as the pump beam and an OPO tunable in the NIR range (720–1000 nm) as the Stokes beam. The spectral resolution of the PARC/PTRC technique was limited to the bandwidths of the OPO and Raman shifter radiation at levels of ~ 12 cm^{-1} . Navigation of the laser beams were controlled with the high-resolution (300 nm) TDM module.

PA waves were detected with an 3.5-MHz, 5.5-mm-diameter, ultrasound transducers (model 6528101, Imasonic Inc., Besançon, France; and a 2.25-MHz, 8-mm-diameter model V323-SM; Panametrics). Signals were then amplified (model 5660C; band, 2 MHz; gain, 60 dB; Panametrics) and recorded with a Tektronix TDS 3032B oscilloscope and a computer using standard and customized software. Ultrasound gel or warm water was used to provide acoustic and optical matching between the samples (e.g., microscopic slides) and the transducers.

PA methods were integrated with PT methods described previously [26]. The temperature rise associated with the energy transfer produced an expansion of the heated volume and a refractive index change. While in PT imaging (PTI) mode, laser (OPO)-induced temperature-dependent variations in the refractive index were visualized with the multiplex thermolens [33] technique using a second, collinear laser pulse from a Raman shifter (see above) at a tunable delay of 0–10 μs , and a CCD camera (AE-260E, Apogee Inc.) [26]. The pump and probe beams had stable, Gaussian intensity profiles and adjustable diameters in the ranges of 10–40 μm and 10–25 μm , respectively. Spatial resolution was determined by the microscope objective (e.g., 0.7 μm at $20\times$, NA 0.4; 300 nm at $60\times$, NA 1.25). While in PT thermolens mode, a laser (OPO)-induced refractive heterogeneity, called a thermolens effect, caused defocusing of a collinear He-Ne laser probe beam (stabilized He-Ne laser model 117A; wavelength, 632.8 nm; power, ~ 3 mW; Spectra-Physics Lasers Inc.) that led to a reduction in the beam’s intensity at its center detected by a photodiode (C5658, Hamamatsu Corp.; and PDA55, Thorlabs Inc.). All signals (PA, PTI, and PT thermolens) were normalized to the laser pulse energy and measured with a power meter [Fig. 1(c)].

Laser radiation was delivered to the samples with either a microscope or an optical fiber [Fig. 1(c)–1(d)]. Pump and Stokes beams with the same horizontal polarization were

combined by a dichroic mirror and focused by a microscope condenser onto 120- μm -thick slides holding liquid samples or cells and CNTs in suspension. We also used an outside microscope scheme with the pump and Stokes beams after the OPO and Raman shifter, through the use of additional mirrors, were focused by lenses L1 and L2 (focal length of both, ~ 6 cm) from opposite directions into the center of the $2\text{ mm} \times 2\text{ mm} \times 2\text{ cm}$ optical cuvette (3G10, Precision Cells Inc.) [Fig. 1(e)]. Spatial overlapping of the laser beams was achieved by use of a tiny hole in thin Al film produced by ablation with a high-energy pump beam delivered into the center of the cuvette. The hole was used to align the Stokes beam with the use of diaphragms D1 and D2 and telescopes T1 and T2 [Fig. 1(c)]. The transducer was partially immersed into the liquid inside the cuvette at a distance of ~ 5 – 6 mm from the focal volume of the laser beams. For PT thermolens detection, the probe beam from a CW He-Ne laser was focused into the focal volume of the pump and Stokes beams by lens L3; a PT thermolens signal was detected by focusing of the probe beam by lens L4 onto a photodetector with a pinhole [Fig. 1(e)]. The probe beam was directed perpendicularly to the pump and Stokes beams, thus allowing the highest spatial resolution (1 – $2\ \mu\text{m}$) to be achieved, as well as a reduction in the influence of background signals from scattered light.

Experimental results

PA Raman spectroscopy of benzene and acetone

To test and verify the PA/PT Raman setup, we first measured the PA Raman spectra (PARS) in acetone [Fig. 2(a)] and benzene [Fig. 2(b)], which have well characterized Raman spectra [10–12]. Acetone spectra were obtained by both tuning the frequency of the OPO, as a pump beam in the visible range from 19011 cm^{-1} (526 nm) to 18248 cm^{-1} (548 nm) at a fixed wavelength of the Stokes beam, $15,649\text{ cm}^{-1}$ (639 nm), and by tuning the frequency of the OPO as a Stokes beam in the NIR range from $12,048\text{ cm}^{-1}$ (830 nm) to $13,157\text{ cm}^{-1}$ (760 nm) at a fixed wavelength ($15,649\text{ cm}^{-1}$) of the pump beam. PARS of benzene were obtained by tuning the frequency of the OPO as a Stokes beam in the NIR range only. Spectral data for each substance were acquired in 4 minutes and consisted of points separated by 12 – 30 cm^{-1} . Figure 2(a) demonstrates that a nonlinear PA signal at two beam excitations are large enough above the linear PA background generated by a beam only. The spectral position of the peak for benzene in Fig. 2(b) in the range of ν_R 3040 – 3070 cm^{-1} is approximately in line with available data on the Raman shift maximum $\nu_R \sim 3059\text{ cm}^{-1}$ [11]. However, we observed that the PA spectra width was greater than the Raman width (20 cm^{-1} [11],), which can be explained by the limited spectral resolution of our setup (12 – 15 cm^{-1}), and possibly an influence of linear background absorption as seen in the range of 2800 – 3200 cm^{-1} .

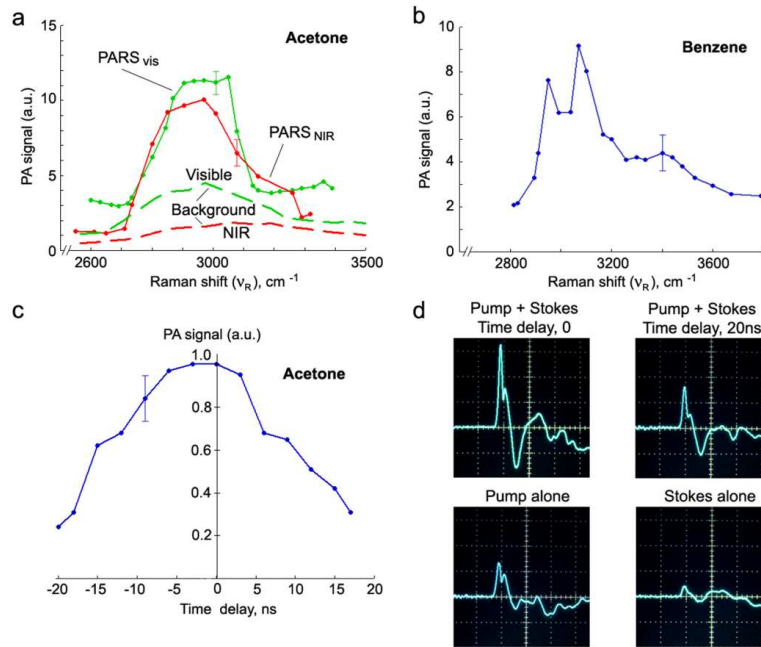


Fig. 2. PA Raman signals in liquids obtained with parallel polarization of the pump and Stokes beams. (a) PA Raman spectra (PARS) of acetone obtained in a thin (120 μm) microscope slide by scanning of first beam in the visible spectral range (PARS_{vis}) and in the NIR range (PARS_{NIR}) at a fixed second beam wavelength of 639 nm (15,649 cm^{-1}). Dash curves show linear PA background during spectral scanning of first beam alone (i.e., without second beam at 639 nm). (b) PA Raman spectra of benzene obtained in a microscope slide at a fixed pump wavelength of 639 nm and spectral scanning of a Stokes beam in the NIR range. (c) PA signal amplitude as a function of delay time between the pump and Stokes beams for acetone. (d) PA Raman signal for acetone at delays of 0 (top, left) and 20 ns (top, right), compared to signals induced by the pump (bottom, left) and the Stokes (bottom, right) beams alone. Amplitude and time scale: 10 mV/div and 1 μs /div.

In this study, to avoid possible damage of the biological samples (see below), we selected a relatively low laser energy level in the range of 20–100 μJ , which was one to two orders of magnitude lower than the energy level used in early Raman-related experiments [10–12]. Nevertheless, we found that this energy level was sufficient to detect nonlinear PA signals. A low energy level, however, leads to a more profound influence of linear background signals in the presence of absorption at the pump and Stokes beam frequencies. This can be explained by the quadratic dependence of nonlinear PA Raman signals on the laser energy levels (i.e., $\sim E_S E_P$), whereas linear signals are linearly proportional to the laser energy level [see Eq. (1)]. This demonstrates the high sensitivity of the PA setup, on the one hand, and the necessity to pay attention to the linear background signals, on the other. In the presence of background signals, the nonlinear PA Raman signal was calculated as the difference between the total PA signal amplitude achieved with both beams and the sum of the linear pump and Stokes PA signals. Measurements of PA signal amplitudes, as a function of the pulse laser energy levels of both beams, revealed a signal linearity in a broad energy range up to 1 mJ. Because PA/PT Raman effects are critical to temporal, spatial, and spectral confinement of the pump and the Stokes beams, the presence of the Raman component in total of the PA signals [Eq. (1)] was verified through a significant reduction (3–10-fold, depending on spectral ranges and laser energy levels) of the PA signal amplitudes at transverse and axial misalignment of the focused pump and Stokes beams in the focal region (i.e., with exclusion of their spatial overlapping), or through the introduction between the pump and Stokes beams of a delay greater than the pulse width (i.e., >12 ns), or the spectral shift outside the Raman transition.

For example, Fig. 2(c) shows that the PA signal amplitude in acetone decreased as the time between the pump and probe beams increased. The total nonlinear signal amplitude at 0 delay time at $\nu_R = \nu_P - \nu_{st} = 2930 \text{ cm}^{-1}$ (corresponding to the maximum Raman shift of 2930 cm^{-1} [11]) [Fig. 2(d), top left] was notably higher than the signal amplitude at a 20-ns delay [Fig. 2(d), top right], and the sum of the linear signal amplitude induced by the pump beam [Fig. 2(d), bottom, left] at $\nu_P = 538 \text{ nm}$ ($18,587 \text{ cm}^{-1}$) and the Stokes beam [Fig. 2(d), bottom right] at $\nu_S = 639 \text{ nm}$ ($15,649 \text{ cm}^{-1}$) separately. The similar control procedures were performed by changing the spatial, temporal, and spectral confinements of the laser beams for all samples below to distinguish nonlinear from linear PA Raman signals at the frequencies ν_P and ν_S . In selected experiments, a change in depolarization from a parallel orientation also led to a decrease in PA signals, which was in line with previous data [11].

PA Raman spectroscopy of olive oil

After evaluating the setup parameters with conventional samples with well characterized Raman spectra, we applied the PA/PT Raman technique to estimate the level of nonlinear Raman signals in olive oil droplets in water. In the first part of this experiment, the system was calibrated with microdroplets of pure oil in water. The linear signal amplitude profiles in olive oil (as in many other vegetable oils containing lipids), ranging from 2750 to 2950 cm^{-1} , represent a superposition of several vibrational states of symmetric and asymmetric CH_2 and CH_3 stretching vibrations with the maximum at $2850\text{--}2885 \text{ cm}^{-1}$ [27,28]. PARS were measured at two set frequencies of the pump and Stokes beams and at the same Raman shift in a tuning range between 3050 cm^{-1} and 2750 cm^{-1} . Specifically, the pump wavelength ν_P was tuned in the visible range between 520 nm and 540 nm at a fixed ν_S of 639 nm , and the Stokes wavelength ν_S was tuned in the NIR range between 770 nm and 823 nm at a fixed ν_P of 639 nm . Two wavelengths set at a ν_P of 539 nm ($18,534 \text{ cm}^{-1}$) and a ν_S of 639 nm and a ν_P of 639 nm and a ν_S of 783 nm corresponded to a maximum Raman shift in lipid of $\nu_R \sim 2885 \text{ cm}^{-1}$. As one can see from Fig. 3(a), both ranges of PA Raman spectra were similar, although in the NIR range lower background absorption was observed as a result of lower linear absorption at frequency ν_P and ν_R .

The measurement of PA signal amplitude at a changed laser pump energy of 529 nm (corresponding to the maximum Raman scattering spectra) revealed the linearity of PA signals in a broad laser energy range of a few microjoules to $30 \mu\text{J}$ [Fig. 3(b)] and appearance of nonlinear effects at higher energy which can be associated with laser-induced overheating effects, accompanied by nano- and microbubble formation around local overheated zones (see details in [5,8]).

We also demonstrated the capability of our integrated setup to simultaneously record PA [Fig. 3(c), 3(d)] and PT [Fig. 3(e)] Raman signals from the same samples. When the delay was changed from 0 to 20 ns, both signals were observed to behave similarly with decreased amplitude due to the disappearance of nonlinear Raman-related components in the total signals. This feature of the PT signal shape associated with fast laser-induced sample heating and slower cooling of the heated zone due to heat diffusion has already been described [26]. PT data obtained for all samples showed similarities in PA and PT signal behavior during the testing of spatial, temporal, and spectral confinements of the pump and Stokes beams. A perpendicular geometry of the probe and pump/Stokes beams provided relatively high optical resolution of $\sim 20 \mu\text{m}$ but lower sensitivity than the PA technique because of the lower optical pathway. In the microscopic scheme, we used a collinear geometry of the probe and pump/Stokes beams [Fig. 1(c)].

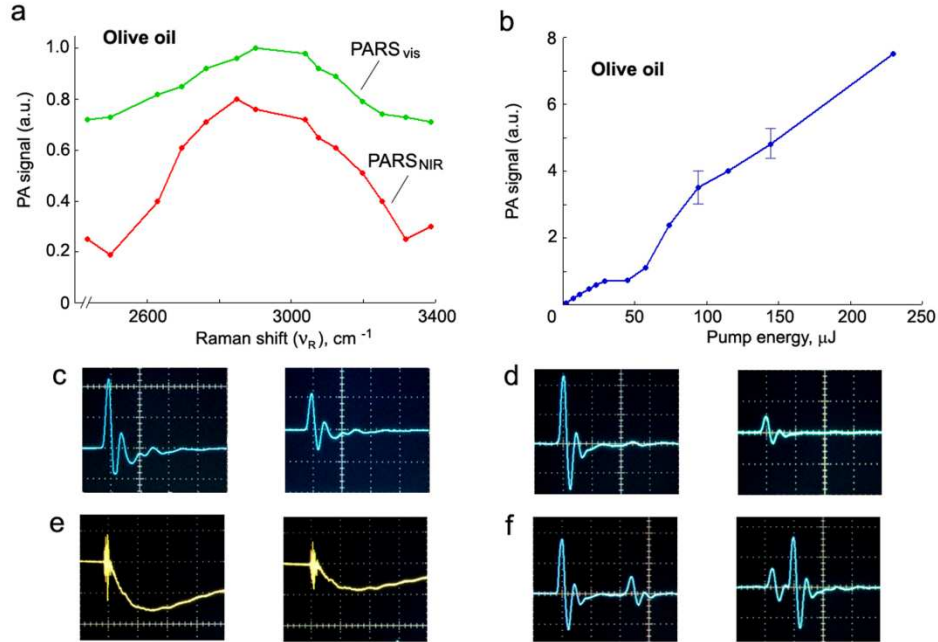


Fig. 3. PA Raman signals in olive droplets in a cuvette. (a) PARS at pump and Stokes beam frequencies in the visible and NIR ranges obtained by scanning at a pump beam wavelength tuned in the visible range and at a fixed Stokes wavelength and by scanning at a fixed pump beam wavelength and at a Stokes beam wavelength in the NIR range. (b) PA Raman signal amplitude as a function of the pump laser energy at 529 nm. (c,d) PA signal amplitude as function of delay time between pump and Stokes pulses with pump wavelengths in the visible (c) and the NIR ranges (d). (e) PT Raman signal at a ν_p of 539 nm and a ν_s of 639 nm at delays of 0 (left) and 20 ns (right). (f) Linear PA signals at delays of 2.5 μ s (left), as well as with a 1-mm distance between pump and Stokes beams (right). Amplitude and time scales: 50 mV/div and 1 μ s/div.

The data in Fig. 3(c)–3(f) confirmed that the total linear signals with no time overlap of pump and Stokes beams (e.g., at a delay of 20 ns) are the sum of the signals induced by pump and Stokes beams alone. The energy level in most of the experiments with olive oil droplets was $\sim 30 \mu$ J at both wavelengths. The minimal diameter of a droplet detectable with a reasonable signal-to-noise ratio (≥ 2) is currently 500 nm.

PA Raman signal detection from carbon nanotubes

As demonstrated in the above experiments, the PARC/PTRC technique can detect nonlinear Raman effects in weakly absorbing (preferential application) samples. In the case of absorbing samples, the influence of background absorption can be excluded by subtracting nonlinear signal from linear signal components at different delay times between the pump and Stokes beams. To estimate this capability of integrated PA/PT techniques to detect nonlinear Raman signals in relatively strongly absorbing samples, we selected CNTs, which we have used as effective contrast agents in *in vivo* flow cytometry applications with both the NIR PT and Raman techniques [24,29]. The Raman spectra of CNTs contain characteristic bands in two spectral regions: the so-called radial breathing modes (100–500 cm^{-1}), which strongly depend on CNT diameter and chirality, and a high wave-number region (tangential and longitudinal modes) between 1200 and 3000 cm^{-1} ; the D band, positioned between 1250 and 1450 cm^{-1} , is associated with vacancies and the presence of other carbonaceous impurities (amorphous carbon, glassy carbon, etc.) that destroy the graphitic symmetry [29]. Band G, lying between 1500 and 1600 cm^{-1} with a maximum at 1593 cm^{-1} , corresponds to the splitting

of the E_{2g} stretching vibrational mode for graphite. This inherent Raman peak with the highest intensity was selected for our study.

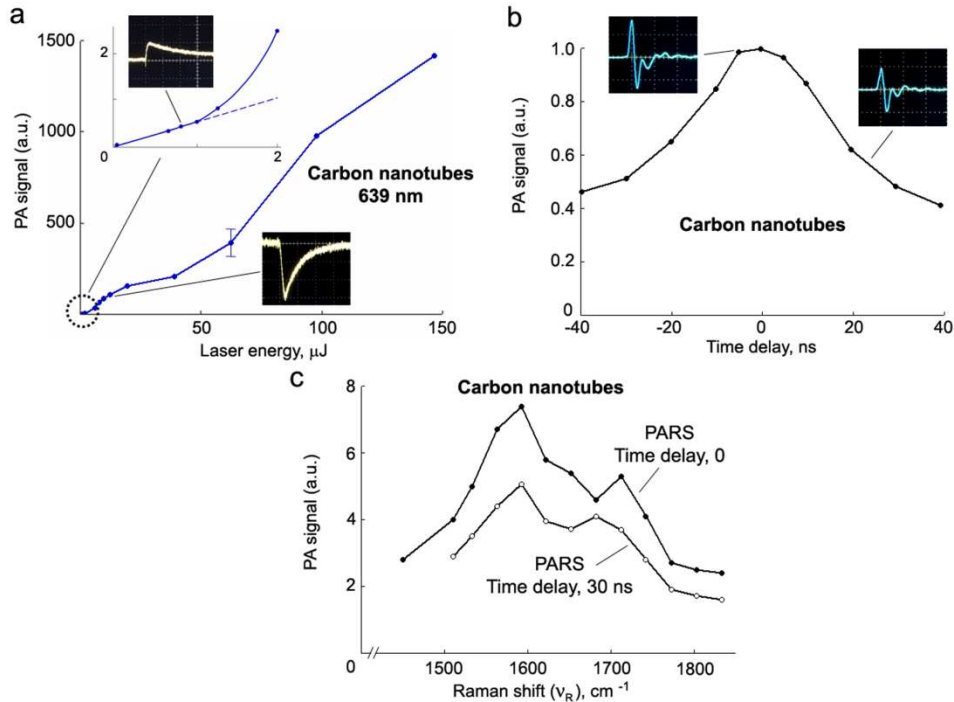


Fig. 4. Linear and nonlinear PA/PT effects in CNTs. (a) PA signal as a function of laser energy. The insets show conventional (i.e., with one-frequency laser excitation) PT signals in linear (left) and nonlinear (right) modes associated with microbubble formation around overheated CNT clusters. (b) PA Raman signal amplitude as function delay between pump and Stokes beams. The inset shows PA signal at delays of 0 (left) and 30 ns (right). (c) PA Raman spectra at delays of 0 and 30 ns between the pump and Stokes beams.

We performed most measurements with CNTs, using protocols similar to those described above for other samples. As the laser energy increased at a frequency of 639 nm and a beam diameter of 20 μm , the four-phase PA signal behavior of CNTs was observed [Fig. 4(a)]: (1) a gradual increase in linear PA signals in the range of 0.1–1 μJ ; (2) nonlinear PA signal enhancement in the range of 1–10 μJ due to bubble formation around overheated CNT clusters accompanied by transitioning the linear positive PT thermolens signals to nonlinear signals with a negative component [Fig. 4(a), left top and right bottom inset, respectively; see other details in [6,24)]; (3) slight saturation of signals in the range of 10–50 μJ ; and (4) “secondary” nonlinear signal enhancement for energy >50 μJ , likely due to thermal explosion of CNTs accompanied by shock waves. To study Raman effects, we selected a relatively low laser energy level, in the range of 10–30 μJ , which nevertheless led to the bubble-formation phenomena. To exclude cumulative effects, each laser pulse irradiated new CNTs by mixing the solution after each laser pulse. Surprisingly, despite strong absorption by CNTs, we clearly observed nonlinear PA Raman signal components that were verified by a decreased signal amplitude as the length of the delay increased [Fig. 4(b)]. As a result, the PA Raman spectra of CNTs were obtained with the maximum that coincides with a Raman shift (1593 cm^{-1} [29],) [Fig. 4(c)]. Repetition of these measurements at a delay of 15–30 ns led to decreases in spectral contrast that were likely determined predominantly by strong linear absorption by the CNTs.

Biological applications of PT/PA Raman technique: detection of cancer cells and chylomicron phantoms in vitro

We have obtained PA/PT Raman signals from biological samples including WTY-1 breast cancer cells, B16F10 mouse melanoma cells, and chylomicron phantom in suspension *in vitro*. The data for most samples were similar. Nonlinear components in PA signals were verified by decreasing the PA signal amplitude with a delay-time increase [Fig. 5(a)–5(c)]. In most measurements, maximum PA/PT Raman signal amplitudes were located at the Raman shift range of 2800–3000 cm^{-1} , which was likely associated with the CH_2 vibrational spectra of lipids with a maximum at 2885 cm^{-1} (corresponding to a pump wavelength of 530–540 nm and a Stokes of 639 nm) present in most cells [30]. In the case of chylomicron phantoms, PA Raman contrast was higher in the NIR excitation range [Fig. 5(c)] compared to the visible range [Fig. 5(b)], which can be explained by the lower linear NIR absorption background. In the case of melanoma cells, we also observed weak signals at a Raman shift of 1580 cm^{-1} . This finding was in line with available data showing that the Raman spectra of melanin demonstrate a strong similarity to those of amorphous carbon, dominated by two peaks centered at 1550 cm^{-1} (1590 cm^{-1} in melanin) and 1350 cm^{-1} (1418 cm^{-1} in melanin) [31]. Recent theoretical models suggest that melanin is composed of much smaller oligomers condensed into nano-aggregates [31].

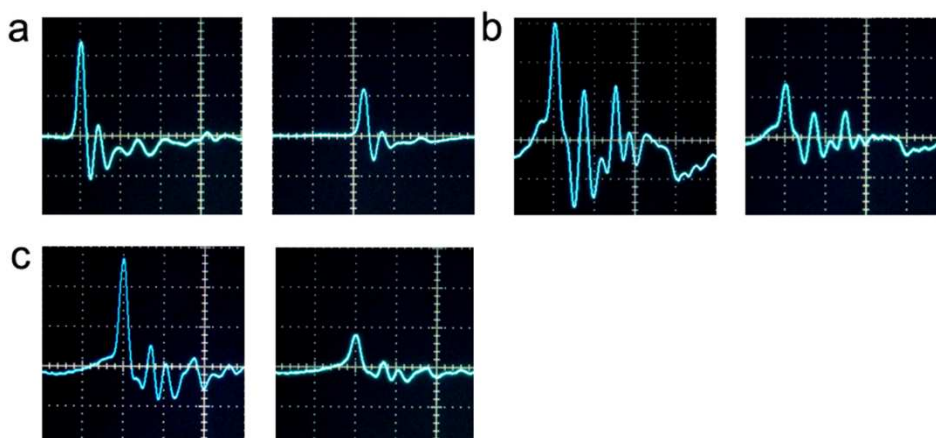


Fig. 5. Linear and nonlinear PA effects in chylomicron phantoms and cells *in vitro*. (a) PA signal in breast cancer at delays of 0 (left) and 20 ns (right). (b,c) PA signals in 200-nm chylomicron phantoms at delays of 0 (left) and 20 ns (right) in the visible (b) and the NIR (c) spectral ranges.

PT Raman imaging of adipocytes in vivo on the animal model

We obtained PT/PA signals and PT images of single adipocytes *in vivo*, using a mouse mesentery model [Fig. 6(a)]. The mesentery is an almost ideal biostructure for proof-of-concept of PARC/PTRC *in vivo* because it consists of very thin (7–15 μm), transparent low-scattering connective tissue with a single layer of blood and lymph microvessels and a clearly distinguishable single layer of adipocytes on the margin of the adipose tissue [25]. From the margin to the deep adipose tissue, adipocytes form a single monolayer consisting of cell clusters and then multilayer structures. A broad distribution of adipocyte sizes was observed by conventional transmission microscopy, ranging from 10 to 70 μm , with the major cell size up to 50 μm , depending on age and location (e.g., in the center of the fatty tissue or at its boundary). PT images were obtained in nonlinear Raman mode with two-beam NIR excitation at 783 nm and 639 nm, with the attenuated beam at 639 nm used as a probe beam in PTI mode at 0 delay time [Fig. 6(b)] and in linear mode with the pump laser beam at a wavelength of 550 nm and a probe beam at 639 nm and a 30-ns delay time [Fig. 6(c)],

assuming in the first case the PT Raman and in the second case the conventional PT image nature, respectively [26]. Indeed, PT Raman images revealed no structures due to large lipid droplets inside the cells, findings that are in line with data obtained by coherent anti-Stokes Raman scattering (CARS) spectroscopy [32]. Conventional PT images demonstrated tiny elongated structures associated with absorption by mitochondrial cytochromes in the visible spectral range [33]. As an additional control, at a delay time of 20 ns between pump (639 nm) and Stokes (783 nm) beams, PT Raman images almost disappeared due to the decrease of PT Raman effects and the absence of strong absorption from lipids and cytochromes in a NIR range. Typical image-acquisition times were on the order of 0.1 s. In analogy to previous protocols with different delay times, we obtained PA Raman signals from single adipocytes demonstrating similar behavior *in vitro* [Fig. 6(d)] and *in vivo* [Fig. 6(e)], with the signal amplitude decreasing as the delay increased from 0 to 20 s.

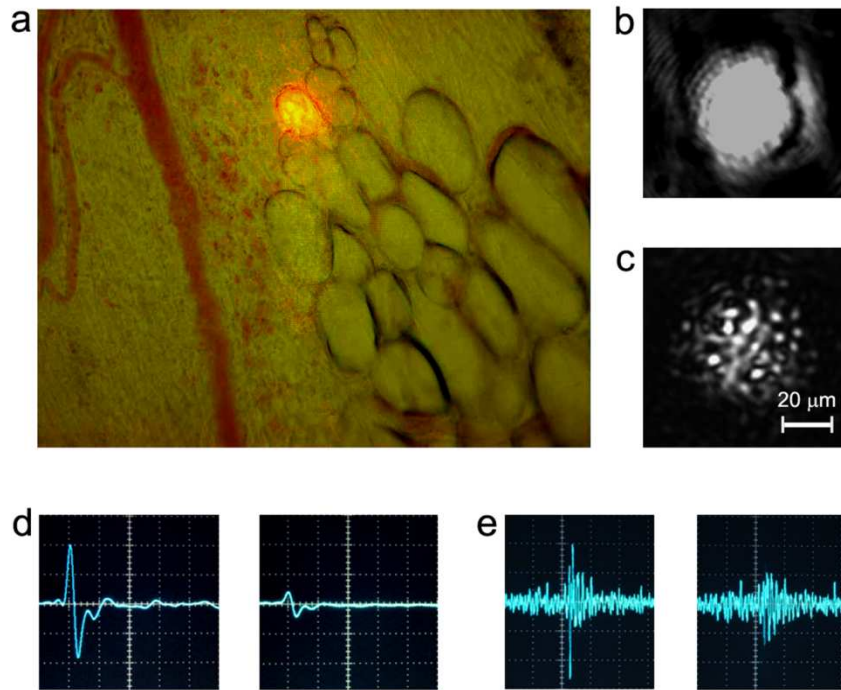


Fig. 6. PA/PT detection of adipocytes *in vivo* in a mouse mesentery model. (a) Mouse mesentery with single layer of adipocytes and the He-Ne probe beam. (b) PT Raman image of a single adipocyte *in vivo* using two wavelengths: 835 nm as pump (30 μ J) and 639 nm (25 μ J) as Stokes wave. (c) Conventional PT image of a single adipocyte *in vivo* using a 550 nm (50 μ J) for heating of cellular cytochromes, and 639 nm, as probe beam (10 nJ) at 30-ns delay [26]. (d) PA Raman signals from adipocytes *in vitro* at delays of 0 (left) and 20 ns (right). (e) PA Raman signals from adipocytes *in vivo* at delays of 0 (left) and 20 ns (right). The signal oscillations are associated with reflections of acoustic waves in the cuvette. The time scales: 1 μ s/div (d), and 10 μ s/div (e).

Discussion

Features of the PARC/PTRC technique

In this work, we focused on demonstrating a new integrated biophotonic platform with the robust optical schemes and nanosecond lasers for PA/PT Raman spectroscopy, cytometry, and imaging *in vitro* and *in vivo* at single cell level. The PT method can be used simultaneously with the PA technique, as these techniques supplement each other, or the PT method can be used as an alternative in some applications, particularly because of its higher

spatial resolution in an imaging mode at the level of 300 nm [33]. We believe that the photothermally induced nano- and microbubbles as a PA/PT signal amplifier can enhance the detection sensitivity of PT/PA Raman cytometry. Indeed, if the temperature of the heated zone under two-wavelength laser excitation in linear mode (e.g., when the pump and Stokes pulses are not overlapping) is close to the boiling point of water, even small additional Raman-related energy depositions (at 0 delay time) may increase the temperature a little above the evaporation threshold, which is accompanied by sudden bubble formation leading to significant (10-50-fold) PT and PA signal enhancement [5–8]. In other words, bubble-induced nonlinear PA signal amplification can be used as a very sensitive indicator of nonlinear PT/PA Raman effects.

Although our present system is not optimized and has a spectral width of 12 cm^{-1} , this resolution still exceeds the resolution of existing Raman methods using ultrafast (e.g., femtosecond) lasers with a broader spectral width. In addition, in cytometry applications, which focus primarily on cell detection and identification, spectral resolution is not too critical unless it is less than the line width of the excited Raman transition (typically $10\text{--}20\text{ cm}^{-1}$) [30]. Nevertheless, the bandwidth of our system can be improved up to $3\text{--}5\text{ cm}^{-1}$ for spectral identification of targets with narrow Raman line widths. The spatial resolution of PA/PT cytometry in detection mode is also not critical and should be comparable with sizes of targets (typical cell diameters in the range of $5\text{--}30\text{ }\mu\text{m}$). Identification of intracellular structures, however, may require higher resolution, and this can be achieved in PTI mode [Fig. 6(b), 6(c)]. PA/PT Raman contrast, representing the ratio of nonlinear PT/PA Raman signals to linear PT/PA background signals, increases synergistically with increases in the pump and Stokes laser pulse energy level, while background signals are proportional to the laser energy levels at the frequencies of the pump and Stokes beams. For example, PA Raman contrast increases approximately 6 times with simultaneous increased in the pump and Stokes pulse energy levels from $50\text{ }\mu\text{J}$ to 2 mJ . A high energy level, however, can lead to photodamage of biological tissues. That is why we explored the possibility of using relatively low energy levels, which in our experiments were $10\text{--}20$ -fold lower than those used in previous studies by others [10–12]. As we demonstrated, linear background signals can be subtracted from total signal, if necessary.

A Raman-active transition may occur for biomolecules having no or a weak infrared spectrum because the PA Raman signal is related to changes in polarizability of these biomolecules and not to the presence of a transition dipole moment [12]. This makes PARC particularly attractive for label-free detection of molecules lacking an NIR or infrared spectrum.

Comparison with existing Raman technique

Most existing Raman techniques, especially CARS spectroscopy, have received much attention as microscopic methods with spectroscopic resolution (e.g., [28,32,34,35] and references there). As has been pointed out since its first application [10–12], the PARC and, as we have demonstrated, the PARC/PTRC method have several potential advantages over other stimulated Raman techniques. CARS spectroscopy requires a very stable laser to accurately measure the intensity of the Stokes beam; in contrast, the PARC technique is free of this requirement because it directly monitors the small amount of heat deposited in the sample. Because the PARC/PTRC technique does not depend on the nonresonant susceptibilities, it is more suitable for cytometry applications. Thus, the fundamental difference between PARC and CARS is that in PARC the energy deposited in a sample is detected directly rather than, as in CARS, through a change in output light intensity. The experimental apparatus needed for the PARC technique is simple (much less sophisticated than that for conventional Raman-gain measurements). Our setup uses only a standard microscopy component. Unlike in CARS microscopy, laser intensity control is not essential because possible intensity fluctuations do not reduce the detection capability or image quality.

In addition, at the nanosecond scale, temporal overlapping of the 1-m-long light pulses in the sample plane is easily achieved. Ultrashort (pico- or femtosecond) laser pulses with high peak power are needed for efficient signal generation in CARS spectroscopy. The strong intensity at the focal center induced with the use of such laser pulses may cause photodamage of biological tissues, which can be avoided with PARC using nanosecond pulses with a relatively low energy output. The noise in PARC arises primarily from thermal fluctuations, and these can be reduced by controlling macroscopic medium parameters, unlike in other Raman processes in which noise arises from microscopic quantum fluctuation, which is harder to control [12].

Potential applications

In general, PARC/PTRC techniques offer several advantages: (1) phase matching of the pump and Stokes beams is not required for PARC/PTRC as it is in CARS [28,32,34,35]; (2) the wavelengths of the pump and Stokes beams can be in the NIR range, in which biological samples are relatively transparent; and (3) adjusting the differences between the two beams allows tuning to different vibrational modes that are not viable for direct laser excitation (i.e., linear mode). The biomedical applications of PARC/PTRC can be similar to those of CARS spectroscopy, but with better sensitivity and a simpler schematic. Applications can also include new, unique tasks. As is clear from the above analysis, Eq. (1), and our preliminary results, the PARC technique can provide (1) Raman scattering spectroscopy (by a change in the wavelength of at least one laser beam), including potential measurement of Raman frequency, cross-section, and gain; (2) detection of nonabsorbing or weakly absorbing structures in the visible, NIR, and even infrared ranges by selection of the difference ($\nu_p - \nu_{st}$) coinciding with the vibrational transition of cell components; and (3) enhancement of sensitivity for detecting cells by the use of both linear and nonlinear signal components. In the second application, linear signals introduce an undesired background that can be minimized by the selection of frequencies of the pump and Stokes lasers in a range with the lowest resonance absorption. This will increase the sensitivity of detecting weakly absorbing cells, such as adipocytes or chylomicrons, in the presence of low background signal from surrounding tissue. In the third application, however, in order to increase both sensitivity and specificity, the frequencies of the pump and Stokes waves can provide strong linear PA signals due to resonance absorption.

In analogy to CARS spectroscopy, targets for the PARC/PTRC technique can be biological samples with lipid-rich, Raman-active fatty acid molecules, which generate strong Raman signals at the CH_2 vibrational mode near $2840\text{--}2860\text{ cm}^{-1}$. Potential applications include label-free detection and imaging of lipid-rich metastatic cancer cells with chemical selectivity, differentiation between various vegetable oils at the signature of the weak = C-H stretching vibration [28], studies of adipogenesis and metabolic lipid disorder, mapping of the distribution of dense cellular proteins (by tuning of the Raman shift to the amide I vibration at 1649 cm^{-1}), and identification of saturated and unsaturated fatty acids in cells [28]. A relatively new application, as we demonstrated here, may include detection and identification of individual cells *in vivo* in static and, potentially, flow conditions in blood and especially in lymph flow in the presence of a strongly scattering or autofluorescent background where spontaneous Raman scattering cannot be easily performed. Targets may include chylomicrons, lipid droplets (e.g., in mature adipocytes), liposomes, and various nanoparticles with strong Raman signals [29], including SERS (surface-enhanced Raman scattering)-active nanostructures. In analogy to application of CARS spectroscopy for study of fat distribution in single cells [32], we believe that our technique can achieve similar results *in vivo* with the potential advantage of being able to use a low laser energy level that is safe for biotissues.

Further improvements

The results that we have described were obtained under the non-ideal arrangement. It should be possible to significantly improve the signal-to-noise ratio with a better detection technique that would make detecting and identifying individual lipid drops, chylomicrons, or liposomes quite possible. Molecular targeting would also be possible with the use of functionalized SERS-active nanoparticles.

Quantitative analysis of a cell population in the microscopic scheme is limited by the relatively small field of view of less than a few hundred micrometers, which necessitates time-consuming scanning. Therefore, to increase the speed of cell analysis, the PARC/PTRC technique can be combined with another technique that we developed, PA/PT flow cytometry [6–8], which benefits both cell detection speed with chemically selective cell analysis in a quantitative manner. Use of a higher pulse repetition rate laser [8] (up to 0.5 MHz) with a stable pulse energy should substantially improve the detection limit by permitting more precise subtraction of linear PT/PA signals. As seen from the signal-to-noise ratio values in Figs. 5–6, we should easily be able to detect single cells in circulation and probably single chylomicrons, after further improvements.

Acknowledgements

This work was supported in part by the National Institute of Health grant nos R01EB000873, R01CA131164, R01 EB009230, and R21CA139373, the National Science Foundation grant nos DBI-0852737 and the Arkansas Biosciences Institute. We would like to thank S. Fergusson for his assistance with laser measurements. We also thank the Office of Grants and Scientific Publications for editorial assistance in the preparation of the manuscript.